Electrochimica Acta 349 (2020) 136243

Contents lists available at ScienceDirect

Electrochimica Acta

journal homepage: www.elsevier.com/locate/electacta

High-performance aqueous rechargeable potassium batteries prepared via interfacial synthesis of a Prussian blue-carbon nanotube composite

Samantha Husmann [a, b, 1], Aldo J.G. Zarbin [a, **], Robert A.W. Dryfe [b, c, *]

[a] Grupo de Química de Materiais (GQM), Department of Chemistry, Universidade Federal Do Paraná (UFPR), CP 19081, 81531-980, Curitiba, PR, Brazil
[b] Department of Chemistry, University of Manchester, Oxford Road, Manchester, M13 9PL, UK
[c] National Graphene Institute, University of Manchester, Oxford Road, Manchester, M13 9PL, UK

ARTICLE INFO

Article history:
Received 8 January 2020
Received in revised form
6 April 2020
Accepted 12 April 2020
Available online 16 April 2020

Keywords:
Aqueous battery
Prussian blue
Liquid-liquid interface
Potassium battery
Thin films

ABSTRACT

Aqueous rechargeable batteries are sustainable energy storage devices with the potential to replace the current state-of-the-art organic phase secondary batteries. Electrode materials for secondary batteries are often based on composite structures, which combine an electronically conducting scaffold with an ionic conductor, whose properties define battery capacity. Optimal integration of these components can be challenging: here we describe a novel approach to prepare electrode materials based on growth at the liquid-liquid interface. This is illustrated with the synthesis of a carbon nanotube/Prussian blue nanocomposite as free-standing transparent thin films, which are applied as cathodes for aqueous rechargeable potassium batteries. Prussian blue is synthesized through an acid-induced decomposition of ferricyanide, promoted by an interfacial electron transfer from an organic phase donor (1,1′-dimethylferrocene) under ambient conditions. The interfacial synthesis yields selective growth of cubic Prussian blue crystals on the carbon nanotube walls, enhancing interaction between the ionic and electronically conducting components, and resulting in a self-assembled film at the liquid/liquid interface. The films are readily transferred to flexible membranes and applied as cathodes in an aqueous rechargeable K^+ battery. Coin-cell devices with activated carbon anodes gave a capacity of 47.6 mAh g^{-1} at 0.25 A g^{-1} with an energy density of 33.75 Wh kg^{-1}

1. Introduction

Aqueous rechargeable batteries (ARB) are a promising energy storage technology for grid-scale usage as they combine safety, sustainability, environmental benefits and cost-effectiveness [1–4]. As the cited literature reveals, this area has undergone a renaissance in recent years. The simple replacement of organic electrolytes by aqueous ones avoids the hazard of flammability, which not only increases safety in pre- and post-production, but also facilitates processing and manufacturing, drastically dropping device costs. Besides, aqueous electrolytes are inherently environmentally friendly, have higher conductivities that increases efficiency and present long-term stability [2]. The now established prevalence of organic-based secondary batteries has eclipsed ARB cathodes and anodes for mobile power applications. Even the simple transposition of organic-battery electrodes to aqueous ones requires extensive studies since intercalation rates, ionic radius and stability change significantly. Aqueous electrolytes have a fundamental restriction on cell voltage due to H_2 and O_2 evolution thus limiting electrode materials to those with very slow water electrolysis kinetics, or working potentials lying within the electrolytic window of water [5]. The limited voltage and lack of appropriate materials for ARB are still the main reason for the low energy density that prevents the large-scale application of these devices, hence the development of new electrodes is key to extending ARB technology.

An intrinsic difficulty with the development of secondary batteries, whether aqueous or otherwise, is the requirement to combine material with a high capacity for the intercalation of the

* Corresponding author. Department of Chemistry, University of Manchester, Oxford Road, Manchester, M13 9PL, UK.
** Corresponding author.
E-mail addresses: aldozarbin@ufpr.br (A.J.G. Zarbin), robert.dryfe@manchester.ac.uk (R.A.W. Dryfe).
[1] Current address: INM-Leibniz Institute for New Materials, Campus D2,2 -Saarbrücken, 66,123 Germany.

https://doi.org/10.1016/j.electacta.2020.136243

ion in question, with high electronic conductivity. Such properties are frequently not found in a pure material, meaning that composite electrodes must be prepared. Traditional methods of preparing composite electrode materials, such as the cathode of non-aqueous lithium-ion batteries, involve the mixing of the transition metal-based active materials with conducting additives, frequently carbon blacks, with other materials such as carbon nanotubes [6–8]. Polymer-based binders are almost always incorporated to ensure good contact between the active material and both the carbons and the current collector, although rather empirical, slurry-based methods are used to form these electrode materials. An improved approach would be capable of growing the active material from the carbon-based electrically conducting framework, ideally under ambient conditions, before the resultant composite would be transferred to an appropriate substrate for cell assembly and testing.

In recent years, the class of compounds known as hexacyanometallates (HCMs) has been shown to perform very well as both cathodes and anodes in ARB with different insertion cations and with little lattice expansion [9–11]. The general structure $A_xM_y[M'(CN)_6]_z.nH_2O$ has transition metals M and M' in octahedral coordination with cyanide ligands, where A is a counter-cation intercalated in the porous framework structure. Storage capacity depends on both the electrochemical activity of metallic species and the structural organization. Prussian blue (PB) is the best known HCM, composed of ferric and ferrous species in its structure ($KFe^{III}[F^{II}e(CN)_6]$). As both metallic species are electrochemically active within the aqueous potential window, PB can deliver a theoretical capacity up to 170 mAh g^{-1} [12]. However, due to the fast crystallization of PB, the defect content and the presence of interstitial water severely limits its performance. Moreover, and in common with the oxide materials used as cathodes in lithium-ion cells, PB and other HCM are not electronically conductive and often present low chemical stability, which limits their application as electrode materials [13,14]. Carbon structures can be incorporated to improve both stability and conductivity of these materials: several works on PB composites with graphene and carbon nanotubes (CNTs) present superior performances in many applications [15–20]. The synthetic route has a major effect on PB structural quality, where controlled approaches such as slow release and contact of reactants can produce organized materials with improved properties [21–24].

PB synthesis is generally done through chemical precipitation or electrodeposition starting from a mixture of $FeCl_3$ and $[Fe(CN)_6]^{3-}$ (or $[Fe(CN)_6]^{4-}$). In acidic media (pH < 4.0), $[Fe(CN)_6]^{3-}$ decomposes generating free iron species, allowing PB formation from a single ferricyanide solution [25]. The synthesis from a single precursor allows fine control over PB growth and its structure, due to the slow release of iron species. Yang et al. were the first to describe the use of ferricyanide decomposition to modify an electrode with PB [26]. Later it was verified that the gold electrode actually presented a catalytic effect on ferricyanide decomposition and that PB formation with other electrodes was much slower, limited by reaction kinetics [27,28].

Herein we describe a new strategy, which we believe will be of wide applicability, in which self-assembled CNT/PB thin films are prepared at a liquid-liquid (L/L) interface. The acid decomposition of ferricyanide is explored together with an interfacial electron transfer, between organic phase 1,1′-dimethylferrocene (DMFc) and aqueous phase ferricyanide, that promotes PB formation within a few hours. By adding CNTs to the L/L system, a CNT/PB composite is obtained as a thin film at the interface, with the PB decorating the CNTs walls. The free-standing films are found to be readily deposited over any desired substrate and then shown to be applicable as cathode materials in aqueous rechargeable potassium batteries, presenting excellent performances in both half and full cells.

2. Experimental section

2.1. Chemicals

CNTs used in the composites were synthesized through the CVD method by the pyrolysis of ferrocene according to previous reports of some of us [29]. The following chemicals were used without previous purification: $K_3[Fe(CN)_6]$ (Sigma-Aldrich), KCl (Vetec), 1,1′-dimethylferrocene (DMFc – Aldrich), toluene (Aldrich), hydrochloridric acid (Sigma-Aldrich), activated carbon (YEC-8A, D_{50} = 10 μm). All solutions were prepared with ultrapure water.

2.2. Interfacial synthesis of CNT/PB films

Prior to the synthesis of PB, CNTs were first assembled at the liquid-liquid (L/L) interface by a method previously reported [30]. Briefly, 0.30 mg of CNTs were dispersed in 20 mL of toluene in a probe ultrasound (Cole Palmer) at 40% amplitude for 10 min in pulses of 50 s/10 s (on/off). The dispersion was then magnetically stirred with 20 mL of ultrapure water in a 50 mL round-bottom flask. After 2 h, a self-assembled CNT film is observed at the L/L interface when agitation is interrupted. For PB synthesis, both aqueous and organic phases were removed and replaced by 20 mL of an aqueous solution of 0.1 mol L^{-1} KCl and 1.0 mmol L^{-1} $K_3[Fe(CN)_6]$, pH3 (adjusted with HCl), and 20 mL of 1.0 mmol L^{-1} DMFc in toluene. The system was then stirred for 4 h after which a blue colour is observed (CAUTION: HCN(g) generated during synthesis!). Both the aqueous and organic phases were extensively washed and exchanged by ultrapure water and pure toluene, respectively, while the blue film of CNT/PB remained at the interface. With a pipette, the film was removed from the liquid/liquid interface and then transferred to a beaker containing the desired substrates placed over a glass rod immersed in ultrapure water. The deposition occurs by lifting the rod upwards against the water/toluene interface. A schematic version of the experimental method is presented in Fig. 1. The effect of synthetic parameters was evaluated by varying the amount of CNT, stirring, time of synthesis and pH as presented in Table 1. Sample names refer to changes in reaction conditions (bold in Table 1) compared to the standard conditions (highlighted – C/PB). For preliminary electrochemical measurements and *ex situ* characterizations, the films were deposited onto tin-doped indium oxide (ITO) glass substrates. For the coin cell devices, films were deposited over pre-weighted PVDF membranes (Merk Millipore® VVLP01300 0.1 μm pore size). All films were dried at 70 °C for 1 h.

2.3. Characterization

Electrochemical measurements were performed on an Autolab PGSTAT100 (Metrohm) using a standard three-electrode setup with an Ag/AgCl (KCl 3 M) reference electrode, Pt wire counter electrode and the as-prepared films as working electrodes. For charge/discharge normalization and specific capacity calculation, film mass was determined. After deposition the films were vacuum dried and, through the mass difference between the pre-weighted substrate and substrate + film, the mass of the film was calculated. This process was done several times for accurate measurement. For films with no or very little PB formation, the mass of bare CNTs films was used. The calculated masses for the films CNT, C/PB and C+/PB are, respectively, 14.0, 19.2 and 34.6 μg cm^{-2}. Raman spectra were acquired using a Renishaw inVia Raman microscope (RE04) with a μm resolution stage-controlled sample holder, coupled with a 633 nm (1.96 eV) laser at 32 mW power using a 20 × objective.

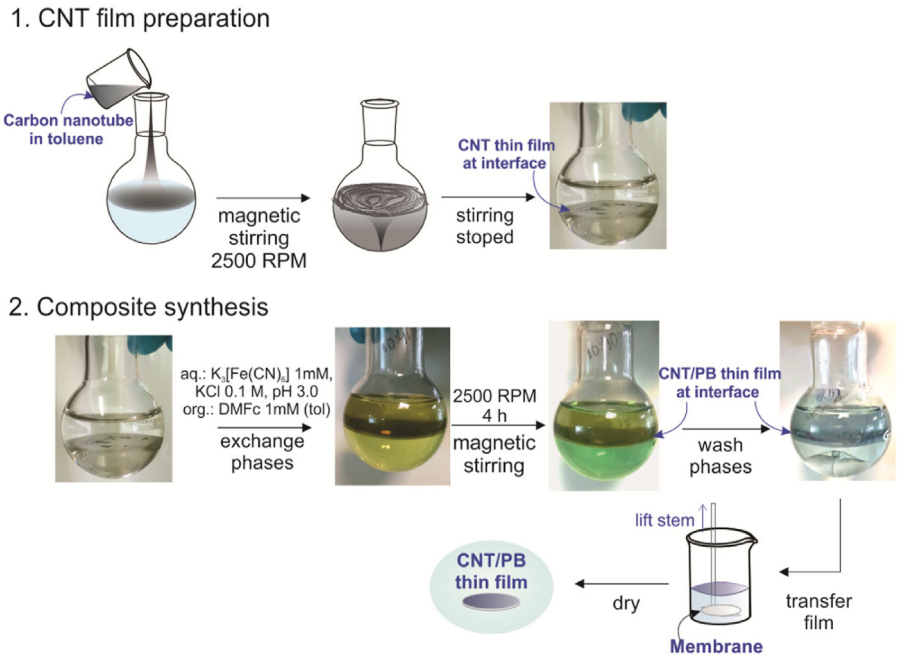

Fig. 1. Experimental steps to prepare CNT/PB thin films at L/L interface.

Table 1
Synthesis conditions of CNT/PB films obtained at L/L interface.

Sample name	[CNT] mg/L	Time/h	pH	Organic phase	Stirring
C/PB	15	4	3.0	DMFc 1 mmol L^{-1} in toluene	Y
C/PB(pH7)	15	4	**7.0**	DMFc 1 mmol L^{-1} in toluene	Y
C/PB(-stir)	15	4	3.0	DMFc 1 mmol L^{-1} in toluene	**N**
C/PB(-DMFc)	15	4	3.0	**Toluene**	Y
C-/PB	**0**	4	3.0	DMFc 1 mmol L^{-1} in toluene	Y
C/PB(-step1)*	15	4	3.0	**CNT 15 mg L^{-1} + DMFc 1 mmol L^{-1} in toluene**	Y
C/PB(24 h)	15	**24**	3.0	DMFc 1 mmol L^{-1} in toluene	Y
C+/PB	**30**	4	3.0	DMFc 1 mmol L^{-1} in toluene	Y

Scanning electron microscopy (SEM) images were obtained with a Quanta 650 FEG microscope (ThermoFisher Scientific) and a Mira FEG (Tescan) at an accelerating voltage of 10 kV. UV–Vis spectra were acquired using a Shimadzu UV-2450 spectrophotometer. A Shimadzu diffractometer (XRD-6000) at CuKα (λ = 1,5418 Å) radiation in low angle mode was used for X-ray diffraction (XRD) analysis. Sheet resistance was measured in a 4 point probe (Jandel Universal Probe) with point separation of 1 mm, the pressure of 10 g/point and currents from 10 nA to 10 μA. Currents were applied in both directions for measurement validation.

2.4. Battery setup

Activated carbon (AC) (YEC-8A) was dispersed in isopropanol at a concentration of 0.05 g L^{-1}. AC electrodes were prepared through filtration of 20 mL of the dispersion onto a pre-weighted PVDF membrane using a syringe pump dispenser (New Era Pump Systems) at a 10 mL h^{-1} rate. Coin cells were built with standard CR2032 case (GELON LIB GROUP). They were assembled by placing a stainless steel spacer over the cell bottom and then the AC and CNT/PB membranes back-to-back with AC facing the current collector (negative side). Another current collector, and then a spring, was put on top of the CNT/PB membrane. A few drops of the 0.5 mol L^{-1} KCl electrolyte were added before closing with the cell cap and sealing with a hydraulic crimping machine (MSK-160D). A photograph of the assembly is presented in Fig. S1 (Supporting Information). The devices were left to rest for at least 12 h prior to testing for electrolyte diffusion and homogeneity through the cell. Coin cells were tested with a CR2032 battery holder with an Autolab potentiostat. All data related to battery procedures and measurements were normalized by the mass of the electrodes obtained by subtracting the mass of the pre-weighed membrane.

3. Results and discussion

In any methodology, PB synthesis depends on the reaction between $[Fe(CN)_6]^{3-/4-}$ and ferric or ferrous species. PB can be prepared by the acid decomposition of $[Fe(CN)_6]^{3-}$ and generation of free iron species, as represented by equations (1)–(3) [25]:

$$[Fe(CN)_6]^{3-}(aq) + 6H_3O^+(aq) \rightarrow Fe^{3+}(aq) + 6HCN(g) + 6H_2O\ (l) \quad (1)$$

$$[Fe(CN)_6]^{3-}(aq) + e^- \leftrightharpoons [Fe(CN)_6]^{4-}(aq) \quad (2)$$

$$[Fe(CN)_6]^{4-}(aq) + Fe^{3+}(aq) + A^+(aq) \rightarrow \underset{PB}{AFe^{III}\left[Fe^{II}(CN)_6\right](s)} \quad (3)$$

The decomposition mechanism and subsequent PB formation are not yet well defined. It has been reported that one of the driving forces for the decomposition is the release of HCN [31]. Nevertheless, it is also observed that there is no formation of the oxidized form of PB (Berlin green – BG) and that the reduction of $[Fe(CN)_6]^{3-}$ or Fe^{3+} (equation (2)) is necessary for PB precipitation, being the limiting condition of the overall reaction since the reduction of such species by water is not thermodynamically favourable [31,32].

The liquid-liquid interface is widely used for interfacial deposition reactions, such as nanoparticle preparation, as well as in electron/ion transfer studies [33,34]. In electrochemical studies at L/L interfaces, two redox couples commonly applied are $[Fe(CN)_6]^{3-}/[Fe(CN)_6]^{4-}$ in the aqueous phase and dimethylferrocenium ($DMFc^+$)/dimethylferrocene (DMFc) couple in the organic phase. The difference in reduction potential means that DMFc spontaneously reduces $[Fe(CN)_6]^{3-}$ at the L/L interface, according to equation (4) [35]:

$$[Fe(CN)_6]^{3-}(aq) + DMFc\,(org) \rightarrow [Fe(CN)_6]^{4-}(aq) + DMFc^+(org) \quad (4)$$

Therefore, in a biphasic system, the presence of organic phase DMFc could promote PB formation through the decomposition of ferricyanide, favoring the reaction presented in equation (2). In order to verify this proposal, 1.0 mmol L^{-1} aqueous solutions of $K_3[Fe(CN)_6]$ at different pH values were monitored over time in the absence and presence of DMFc in toluene through UV–Vis spectroscopy. Fig. S2 shows the photographs of the solutions at different pH values as prepared, and after 24 h (no stirring). The green/blueish colour of the aqueous phase at lower pHs due to PB formation, after 24 h contact with a DMFc solution, is evident. $K_3[Fe(CN)_6]$ has a characteristic band at 420 nm assigned to the ligand to metal charge transfer (LMCT), while PB presents a broad intervalence band between 650 nm and 720 nm [36,37]. The ratio between those absorbances, given by A_{680}/A_{420}, was calculated for the different systems as a function of time (Fig. 2).

As observed in the photographs presented in Fig. S2, both low pH and the presence of DMFc favour PB formation. The ratio profiles indicate that a pH > 3.0 is not acidic enough to promote the reaction either in the presence or absence of DMFc. Nevertheless, at pH 2.0 and 3.0, the effect of DMFc can be already observed in the first hour of the reaction, with more than 100% increase in the intensity of the PB band, compared to the system without DMFc. These studies confirm and demonstrate the effect of DMFc on PB formation through a single ferricyanide solution. Even though DMFc/$[Fe(CN)_6]^{3-}$ are commonly used in interfacial electron transfer studies, the ratio between components is usually much lower (1:100 to 1:10,000 DMFc:$[Fe(CN)_6]^{3-}$) and the extent of ferricyanide reduction by DMFc and PB formation is much more limited. This effect was first observed by Quinn et al. while evaluating organic redox couples for electron transfer at liquid interfaces [38]. A similar observation is briefly described in a previous paper by some of the authors of this work, in which $[Fe(CN)_6]^{3-}$ generated by the interfacial charge transfer reaction between $[AuCl_4]^-$ in organic media and acid $[Fe(CN)_6]^{4-}$ decomposes to form PB as by-product [39]. However, this electron transfer reaction has not been explored to date as a means to deliberately produce and control PB formation at the L/L interface.

Once PB had been synthesized through the proposed interfacial reaction, this system was employed for CNT/PB composite preparation. First, a CNTs film was stabilized at the L/L interface through the interfacial method previously described by some of us [30,40]. Both aqueous and organic phases were then replaced by acidic aqueous ferricyanide solution and DMFc in toluene in order to produce PB (see experimental section). KCl was added in excess to the aqueous phase in order to provide the necessary cations for electroneutrality of the PB structure. Different synthetic conditions were also evaluated. UV–Vis absorption spectra from both aqueous and organic phases remaining after each synthesis, as well as the produced films, are presented in Fig. 3 and Fig. S2. From the spectra, it is possible to analyse the effect of the various synthetic conditions. As previously demonstrated, pH and DMFc have significant effects on PB formation, where the PB band is neither observed in aqueous phases nor in deposited films of C/PB(pH7) and C/PB(-DMFc) syntheses (see Experimental section Table 1 for adopted nomenclature). Stirring was also found to promote PB formation and deposition on the CNTs, favouring contact between phases and interfacial mass transport. In aqueous phase spectra of C/PB(-stir) a high-intensity PB absorption occurs, however, at the film spectra from the same synthesis there is only a slight absorption. Therefore, even though the reaction takes place at the L/L interface, where there is also the CNTs film, without stirring the PB produced does not attach to the CNTs and diffuses through the aqueous phase, being removed during the phase cleaning process.

In the absence of CNTs (C-/PB), it is not possible to produce a PB film at the L/L interface. When stirring is ceased after the synthesis, a blue powder precipitates at the L/L interface. The powder was removed with a pipette and dropped over a quartz substrate and

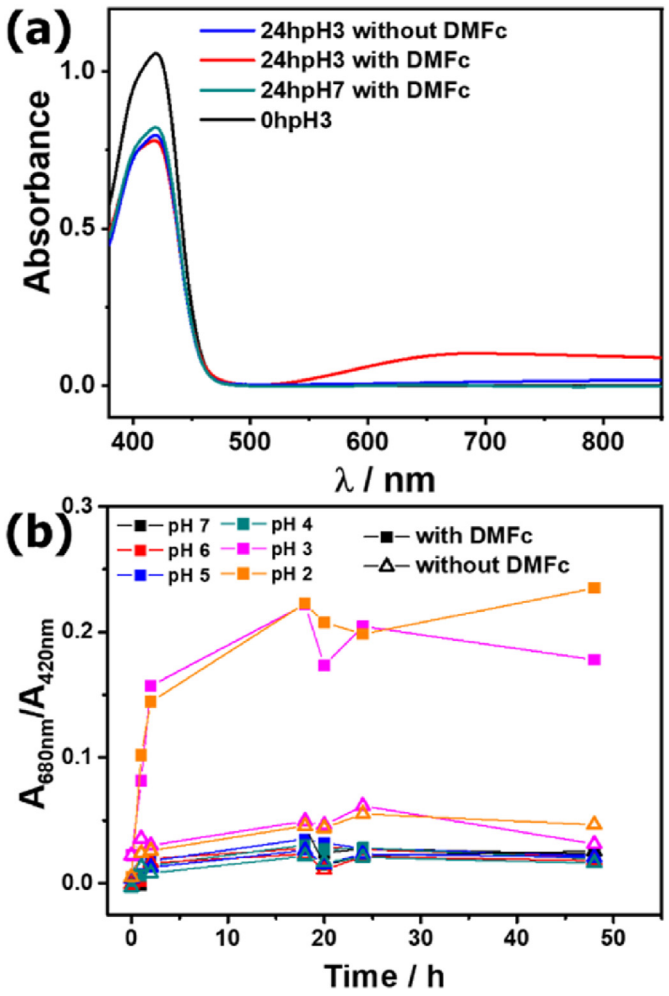

Fig. 2. (a) UV–Vis spectra of $K_3[Fe(CN)_6]$ aqueous solutions and (b) A_{680nm}/A_{420nm} ratios vs. time obtained from UV–Vis spectra at different pHs in the presence (full symbol) and absence (open symbol) of DMFc in the toluene phase of the water/toluene system.

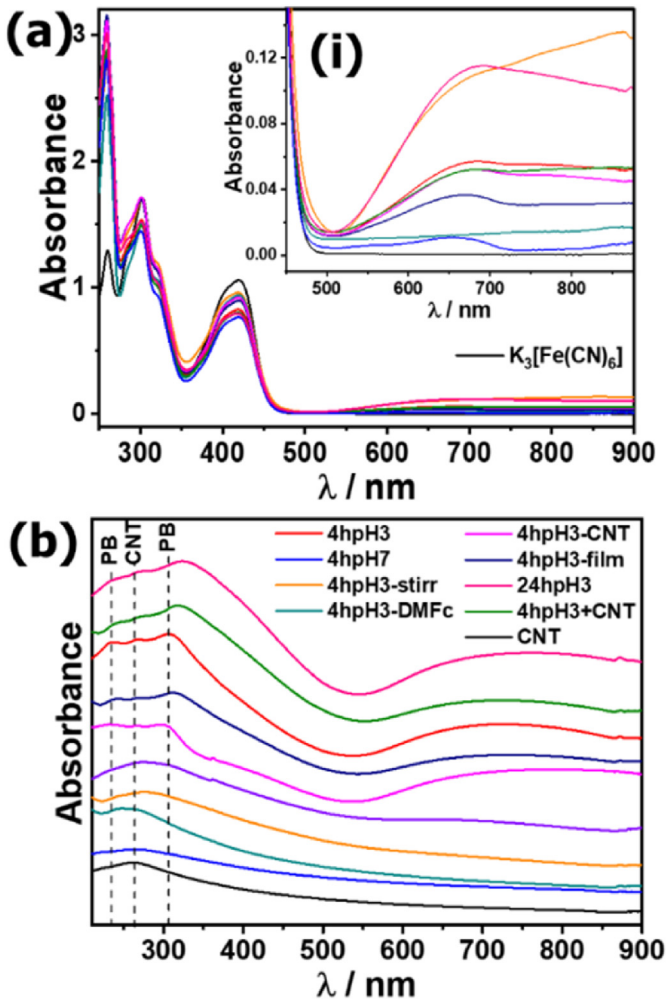

Fig. 3. (a) UV–Vis spectra of (a) the aqueous phase and (b) the films obtained at the L/L interface of different synthesis conditions of CNT/PB composites. (i) Detail of the 500–800 nm region. Spectra in (b) presented in stacking mode to better visualize data.

dried for characterization. It is likely that CNTs act as nucleation seeds for PB, favouring growth on the CNTs walls: a similar effect has been seen with the formation of CNT/conducting polymers at the L/L interface [41]. Increasing reaction time [C/PB(24 h)] produces more PB, though not all of the material is immobilized at the L/L interface, indicated by the strong PB absorption of the aqueous phase.

The effect of step 1 over PB synthesis was also evaluated, that is, the prior assembly of CNT as thin films at L/L interface [C/PB(-step1)]. Therefore, step 1 was omitted and CNTs were added with DMFc in toluene. Both the aqueous phase and film presented lower PB absorption compared to the standard synthesis (C/PB). The prior assembly of CNTs at the interface promotes the reaction, most likely due to their ability to act as sites for product nucleation and their ability to promote electron transfer by conducting electrons from the donor DMFc to the iron complex, even when the two precursors are remote from one another. The effect of the increase of CNT content (C+/PB) could not be clearly evaluated through UV–Vis analysis since the spectra were very similar to the standard synthesis.

According to the proposed mechanism, DMFc acts to promote the reduction of $[Fe(CN)_6]^{3-}$ ions, by oxidizing to $DMFc^+$. The analysis of the spectra of the organic phases (Fig. S3) shows a small decrease in the absorbance of DMFc, denoting its oxidation. $DMFc^+$ can be transferred to the aqueous phase, absorbing at around 645 nm, being overlapped by the PB band [42].

The optical and electrical properties of the composite films were then studied. Fig. 4a shows the transmittance at 550 nm and sheet resistance of the films. Overall, films with lower PB content present higher transmittance, closer to the bare CNT film. C+/PB has much lower transmittance due to the higher amount of CNT, also resulting in lower sheet resistance. Conversely, films with a higher amount of PB, like C/PB(24 h), presented an increase in sheet resistance, since PB itself is not electrically conductive. It was not possible to measure sheet resistance of the C-/PB sample as a continuous film is necessary for this characterization. The films are presented in Fig. 4b: the transparency of the composites, as well as blue shade variation, is observed. As discussed, in the absence of CNTs there is no film, and the powder deposition is very heterogeneous.

The X-ray diffractograms of the films (Fig. S4) present the characteristic peaks from both composite materials. At d = 3.43 Å the graphitic (002) plane from multiwalled CNTs appears. In some samples, like C/PB(pH7), lower intensity peaks assigned to iron and

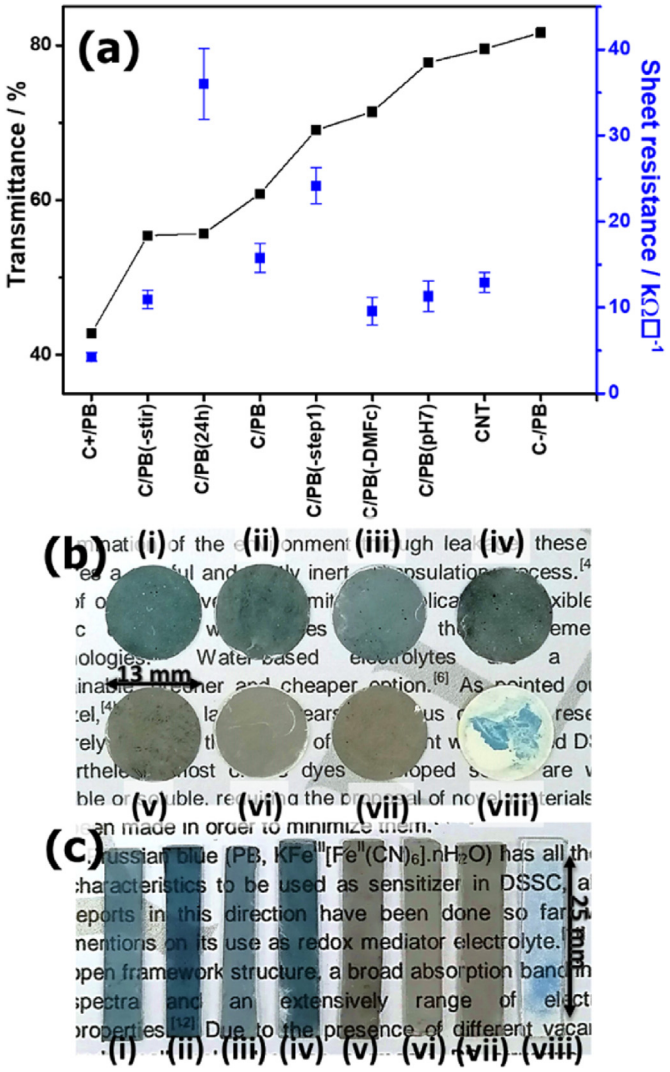

Fig. 4. (a) Transmittance at 550 nm and sheet resistance of the CNT/PB films. (b,c) Photographs of the films (i) C/PB, (ii) C/PB(24 h), (iii) C/PB(-step1), (iv) C+/PB, (v) C/PB(-stir), (vi) C/PB(pH7), (vii) C/PB(-DMFc) and (viii) C-/PB on (b) PVDF membranes and (c) ITO.

iron oxides from the CNT filling are also observed. PB peaks occur at d ≈ 5,21, 3,71 and 2,56 Å, assigned to (200), (220) and (400) planes, respectively. In the samples where PB synthesis is not favoured, those peaks present low intensity or do not appear, confirming the effects of the synthetic parameters.

In the Raman spectra (Fig. 5), three characteristic CNT bands are observed, for the range evaluated: D (ca. 1334 cm^{-1}), G (ca. 1584 cm^{-1}) and D' (ca. 1620 cm^{-1}) bands. The G band refers to C=C stretching from the sp^2 hexagonal network of carbon, typical of graphitic structures. The D band arises from a loss of symmetry in this network due to incomplete bonding and/or sp^3 carbon, while D' is assigned to the edge and outer wall defects on CNTs [43–45]. Besides modes derived from CNTs, C≡N stretching bands from PB cyanide ligands are observed between 2000 and 2200 cm^{-1}. In the syntheses that promote PB formation, there is a small shift of cyanide bands to higher frequencies compared to the bare PB (2148 cm^{-1} for C-/PB to 2156 cm^{-1} for C/PB). This indicates that the charge density on the cyanide ligand is increased in the composite, which is usually assigned to the π-π interaction between CNTs and PB through a π back bonding from CNT into 2pπ* orbitals of CN groups [46,47]. There is also a shift in the G band to lower wavenumber in the films with a high amount of PB, characteristic of n-doped CNTs in which the electronic transfer from the valence to the conduction band is improved (Fig. 5b) [48].

This is not the usual effect observed for CNT/PB composites, especially due to the observed shift in cyanide bands that indicates the opposite behaviour (charge transfer from CNT to PB). Previous work showed that CNT can be n-doped at a polarized L/L interface in the presence of DMFc [49]. Since all composites present a shift compared to the C/PB(-DMFc) (Fig. 5b), a net doping due to the DMFc could explain the observed behaviour. The modification of the CNTs walls by PB can also increase the defect degree due to the loss of symmetry. While no significant changes in I_D/I_G ratio were observed, $I_{D'}/I_G$ varied between 0.15 (C/PB(-DMFc)) and 0.35 (C+/PB), which indicates a non-covalent interaction between CNT and PB (Fig. 5b) [50].

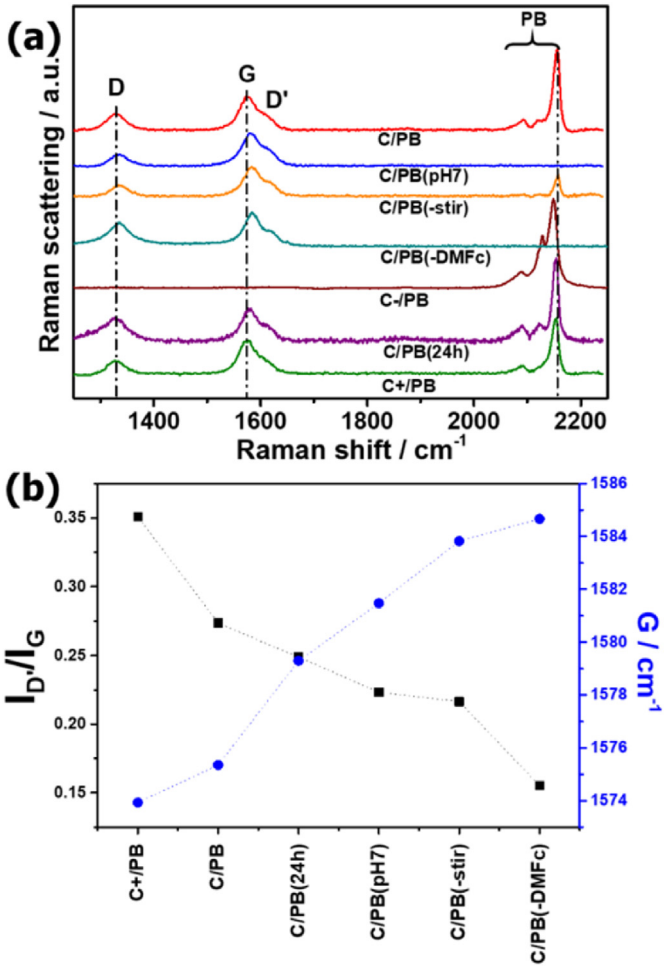

Fig. 5. (a) Raman spectra and (b) $I_{D'}/I_G$ ratio (black) and G band position (blue) of the CNT/PB films. (For interpretation of the references to colour in this figure legend, the reader is referred to the Web version of this article.)

The morphology of the films was evaluated through SEM, presented in Fig. 6. The composites synthesized under favourable conditions for PB formation clearly present the characteristic cubic morphology. PB cubes appear homogeneously dispersed over the CNT film. It is interesting to note that, regardless of the synthetic conditions, PB cubes grow selectively over CNTs walls, while there are no isolated cubes over the substrate. This demonstrates that CNTs act as nucleation seeds for PB growth, facilitating its formation.

The absence of cubes in C/PB(pH7) and C/PB(-DMFc) once again confirms the role of pH and DMFc in the reaction mechanism of $[Fe(CN)_6]^{3-}$ decomposition. Similarly, the contrast between C/PB(-stir) and C/PB(24 h) denotes the effect of both variables in the amount of PB synthesized. With 24 h of reaction, there are larger and agglomerated cubes, with a secondary growth process from the previously formed cubes, as shown by the arrows presented in Fig. 6g. The greater cube size, as well as coalescence of the particles in C/PB(24 h), decreases the contact area with CNTs surface, in agreement with the higher sheet resistance of this film compared to others. In the C/PB(-film) composite, several agglomerated cubes are observed, differing from the C/PB morphology, which demonstrates that the assembly of CNTs film prior to PB synthesis provides a composite that is more homogeneous and with a better distribution of PB particles over CNTs films. It is interesting to point out the homogeneity and nanometric size of the cubes in the absence of CNTs (C-/PB), smaller than 200 nm. Due to fast crystallization, PB synthesized through chemical routes usually presents micrometric size distribution with low crystallinity [22]. Despite the important role of the CNTs in imparting conductivity and stability to the films, the route of PB preparation through the acid decomposition of $[Fe(CN)_6]^{3-}$ promoted by DMFc presented here is an alternative method to obtain pure PB nanoparticles.

We now turn to the electrochemical characterization of the composite films, for which they were deposited over ITO substrates. The powder from C-/PB was dropped and dried aiming at a qualitative characterization of its electrochemical behaviour, however, due to the heterogeneity of the deposit, the response regarding battery performance could not be evaluated. Fig. 7a presents cyclic voltammograms of the films in KCl 0.1 mol L^{-1}. In the films with an appreciable amount of PB, two pairs of redox processes are observed at $E_{1/2}$ ca. 0.20 and 0.85 V, characteristic of the two metallic species in the PB structure. The first set is assigned to the high spin iron species coordinated to nitrogen and water, in the transition between PB and its reduced form, Prussian white (PW). The second pair refers to low spin iron coordinated to carbon, in the transition between PB and BG, as presented in equations (5) and (6) [51].

$$\underset{\text{PB}}{KFe^{III}\left[Fe^{II}(CN)_6\right]}\,(s) + K^+(aq) + e^- \underset{\text{I}}{\overset{\text{II}}{\rightleftharpoons}} \underset{\text{PW}}{K_2Fe^{II}\left[Fe^{II}(CN)_6\right]}\,(s) \quad (5)$$

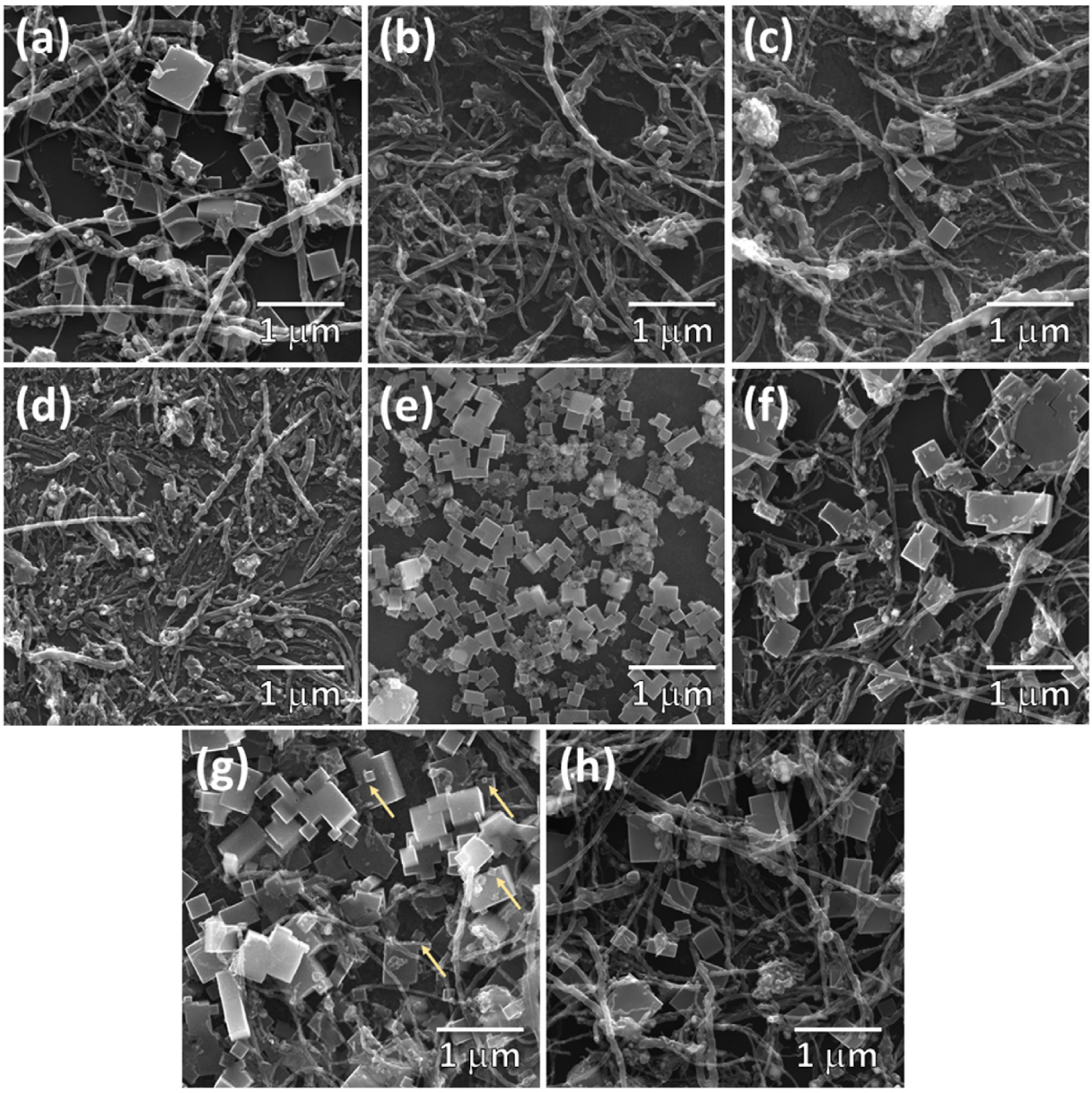

Fig. 6. SEM images of the films (a) C/PB, (b) C/PB(pH7), (c) C/PB(-stir), (d) C/PB(-DMFc), (e) C-/PB, (f) C/PB(-step1), (g) C/PB(24 h) and (h) C+/PB.

$$\underset{\text{BG}}{Fe^{III}\left[Fe^{III}(CN)_6\right](s)} + K^+(aq) + e^- \underset{\text{III}}{\overset{\text{IV}}{\rightleftharpoons}} \underset{\text{PB}}{KFe^{III}\left[Fe^{II}(CN)_6\right](s)} \quad (6)$$

In some voltammograms, there is a small shoulder in the oxidation process from PB to BG. Even though this signal is often observed in many works, it is not usually discussed [52–54]. Nevertheless, different coordination stoichiometries that arise from incomplete coordination, coordination of water, structural rearrangements and other defects can lead to shifts in the redox process of the metallic species [55,56]. In addition, it is likely that partial decomposition of $[Fe(CN)_6]^{3-}$ occurs, generating different aquo and cyano complexes, such as $[Fe(CN)_5]^{2-}.H_2O$ which could take part in PB formation. Therefore, the produced structure can present different $[Fe(CN)_6]^{3-}$ units, since the second redox process is related to carbon coordinated iron. For better observation of the differences between current densities, the charge associated with the PB-PW reduction process (process II) was calculated, as presented in the detail of Fig. 7a.

Of the various composites, C/PB presented the highest current densities, with well-defined reversible processes. As demonstrated in SEM images, this sample has several isolated cubes homogeneously spread over CNTs walls, which is different from other composites that exhibit larger and/or agglomerated cubes, decreasing PB surface area. In the absence of CNTs, the redox processes of PB are distorted by the resistivity of the material, demonstrating the improved effect of CNT on the electrical and electrochemical properties of the films.

Fig. 7b shows charge and discharge curves obtained at 200 mA g^{-1} between −0.20 V and 0.65 V, in order to evaluate the PW/PB process. The films with a significant amount of PB present a well-defined plateau at ca. 0.20 V. Near the upper cut-off potential there is also a slight change in the curve from the observed shoulder in cyclic voltammetry that precedes the second oxidation

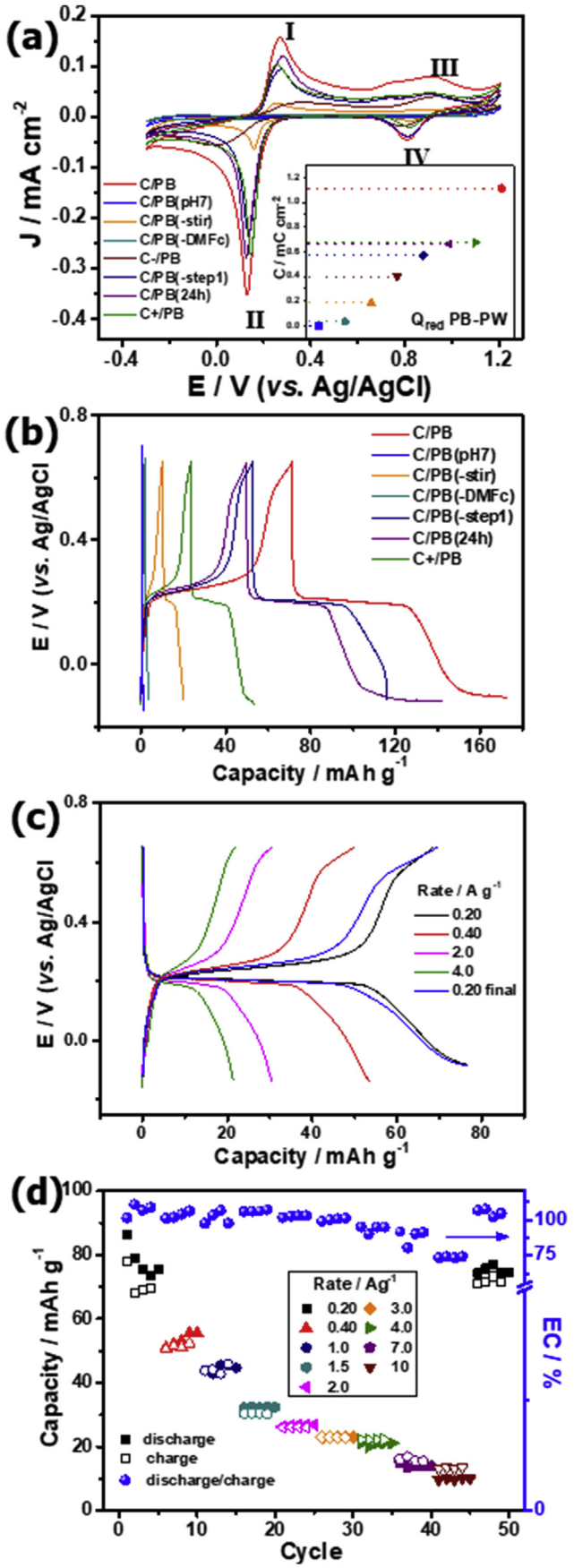

process. Composite C/PB + CNT presents a reduced specific capacity compared to the other composites, due to higher mass/area, since it is prepared with twice the amount of CNTs. This indicated that even though CNTs act as a nucleation point for PB growth, the formation of PB mostly depends on the decomposition rate of $[Fe(CN)_6]^{3-}$. Composites presented capacities ranging from 12 mAh g^{-1} to a significant 75 mAh g^{-1} for C/PB film, which is nearly 90% of the theoretical capacity of 1 electron process for PB. Since C/PB presented the best performance, the behaviour at different current densities was evaluated. Fig. 7c shows the second cycle of some of these charge-discharge curves obtained at different rates. Due to the internal resistance of the material, capacity typically decreases as rate increases. The capacity offset can be better observed in Fig. 7d. With a tenfold increase in the rate, from 0.20 to 2.0 A g^{-1}, there is a 35% capacity retention, while between 0.10 and 1.0 A g^{-1} or 0.70–7.0 A g^{-1}, retention is around 30%. In this context, it should be noted that most of the recent potassium battery reports are performed in organic media.

Aqueous potassium systems are still not very widely explored, however, the existing reports are dominated by the use of PB and analogues as electrode materials [57–59]. The performances of some reported aqueous potassium batteries are summarized in Table S1. Baioun and co-workers described an oxidized PB electrode (the so-called Prussian yellow) that presented 142 mAh g^{-1} at 0.4 A g^{-1}, being the highest value reported for aqueous K-ion batteries. Su and co-workers reported a dehydrated PB electrode with 120 and 70 mAh g^{-1} capacity for $2e^-$ and 1 e^- process, respectively, at 0.20 A g^{-1}. The electrode also presented 96% capacity stability after 500 cycles at 0.50 A g^{-1} [60]. Cui and colleagues have described PB analogues, such as CuHCFe, which present excellent rate cyclability and stability, achieving nearly 60 mAh g^{-1} in a half-cell configuration [61–63].

From Fig. 7d, good repeatability of the measurements is also observed, with little variation of the capacities in the same applied rate. After discharge cycles at different rates, the film was again evaluated at 0.20 A g^{-1}, showing a recovery of 100% of the initial capacity. Nevertheless, from the charge-discharge curves in Fig. 7c a slight change in the profile compared to the initial one is seen, especially in the charge, indicating that there was some structural change within the material.

The coulombic efficiency (CE) is presented in Fig. 7d. Initially, CE is over 100%, which occurs because PB already contains some intercalated cations in its structure that contribute to the initial discharge cycles. Also, it was verified that the reduction of iron species from the CNTs have a small contribution to the overall electrochemical performance which leads to a coulombic imbalance, as we discuss further. Along with the cycles, there is a stabilization of the CE which remains around 100%. At high rates, e.g. 7.0 A g^{-1}, the intercalation processes do not happen efficiently and CE drops to 75%. Nevertheless, CE recovers to 100% in the final cycles.

Once the performance of the composite was evaluated as a half-cell in a three-electrode system, full cells were prepared in a coin cell setup (Fig. S1). Given the potentials of PB redox processes, C/PB films were used as the cathode, with a filtered activated carbon (AC) electrode used as the anode. In order to evaluate the behaviour of the composite, commercial AC was chosen as a standard electrode material with high surface area, low cost and wide operating voltage. Characterizations of AC are presented in Fig S5. Cyclic voltammetry of the AC electrode is presented in Fig. S6a. As

Fig. 7. (a) Cyclic voltammetry (50 mV s^{-1}) with detail in the charge of the process II. (b) Charge/discharge curves at 200 mA g^{-1} of the different CNT/PB films. (c) Charge/discharge curves at different rates and (d) rate handling along cycles with coulombic efficiency of the C/PB composite. Electrolyte: KCl(aq.) 0.1 mol L^{-1} for all measurements.

expected for the carbon material, only a capacitive profile is observed from the electric double layer. Therefore, the device works in an asymmetric configuration with a battery (intercalation) and capacitor-type materials as cathode and anode, respectively. Even though the mass loading of AC is much higher than the composite material (four times mass loading), the capacitive current is still much lower than redox processes from C/PB film, indicating that a higher amount of AC is required to allow full intercalation reversibility in the cathode during charge/discharge processes. The C/PB electrochemical response was evaluated in a two-electrode setup with AC and compared to the standard three-electrode system (Fig. S6b). Due to the charge limitation of AC, the charge density of PB processes drops significantly and broadens. Besides, there is a potential shift of such processes due to the reference change, where the PW-PB transition occurs at $E_{1/2} = 0.52$ V.

For coin cell assembly, the films were deposited over PVDF membranes (Fig. 1). The cells were named as "cathode-anode", hence the battery built with C/PB and AC is C/PB-AC. Fig. 8a shows the representative voltammograms of the device in different windows and cycles. The PW/PB redox process is observed at shifted potentials as expected from the previously discussed voltammetry. Even though the films are deposited over PVDF membranes that are very rough and porous, the redox profile is well defined, which indicates that the electrode materials possess both good ionic and electronic conductivity. When the anodic window is increased to 0.9 V, a secondary oxidation process occurs in the reverse sweep. Such processes gradually decrease during cycles, becoming a small feature that finally disappears after approx. 15 cycles. When a battery is assembled with bare CNT films, the same behaviour is observed (Fig. S7). This was assigned to oxidation of the iron species present inside the CNT cavities, characteristic from the route used to synthesize the CNTs used in this work [29]. These species also affect the charge/discharge profiles, especially at slow rates. As presented in Fig. S8, during the charging process there are potential drops near the cut-off potential that also gradually become less evident leading to a typical charge/discharge profile.

Charge-discharge curves were obtained at different rates (Fig. 8b), where the times were normalized by the mass of the cathode (C/PB) in order to evaluate the composite performance. Even though AC limits device operation, the full cell presented significant capacity values reaching 46 mAh g^{-1} at 0.25 A g^{-1}. Also considering the discharge rates applied in this work, the produced device presented excellent capacity performances, yielding an energy density of 33.75 Wh kg^{-1} at a power density of 194.4 W kg^{-1}: it is likely that the interfacial preparation route contributes to this high capacity.

The first report of a full potassium battery based on PB presented 8 mAh g^{-1} at 0.012 A g^{-1} in an aqueous system, followed by another work with 78 mAh g^{-1} at an extremely low rate of ca 0.0084 A g^{-1} in organic electrolyte [64,65]. Due to the great focus on Na-ion batteries, K-ion batteries have been largely unexplored for several years and it was only recently that another full cell of this type was described, as shown in Table S1. The work by Ren and co-workers based on Ni-PB analogue and $NaTi_2(PO)_3$ presented capacities up to 67.6 mAh g^{-1} at 0.08 A g^{-1} using a mixed K/Na electrolyte [66]. In the work of Cui and co-workers, the Cu-PB analogue device reaches 54 mAh g^{-1} at 0.06 A g^{-1} which is the highest described capacity using only K-ions in a cell based on PB [63]. Besides the PB family of electrode material, Charles and collaborators have described a cell based on vanadium oxide having a high performance of 70 mAh g^{-1} at 2 A g^{-1} [67]. In all these works, electrode materials are first blended with carbon or other conductive additives and binders and further processed by coating methods such as doctor blade. In our work, the composite is

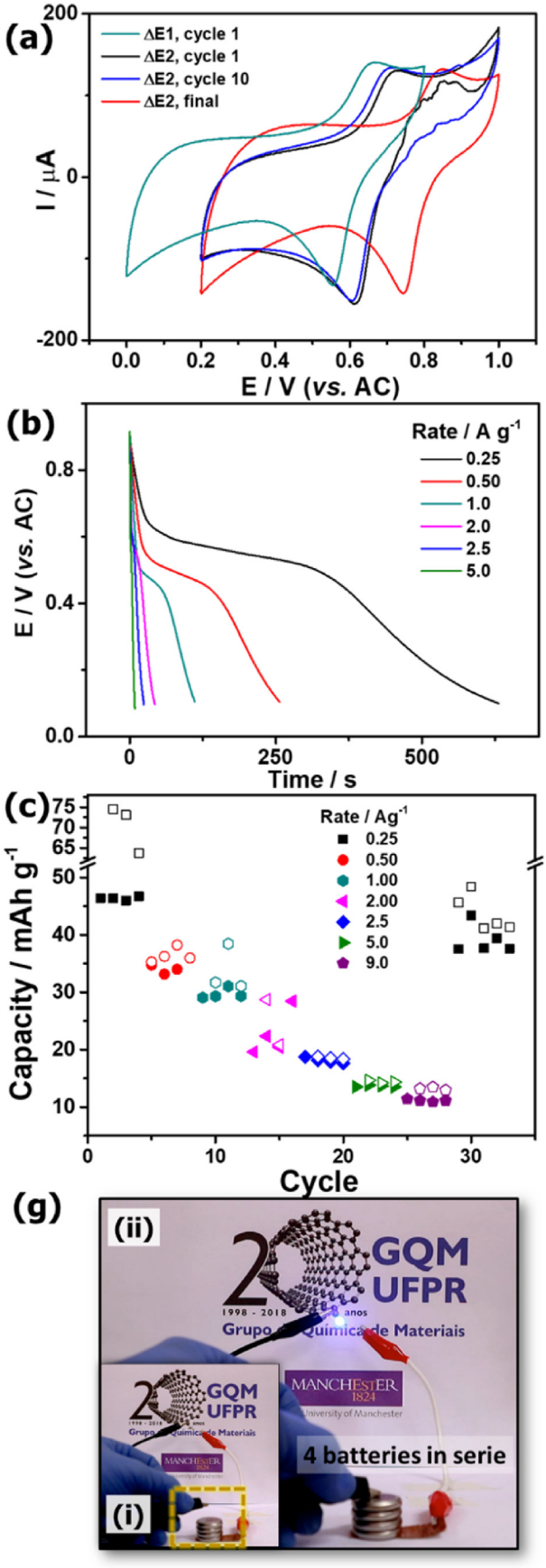

Fig. 8. (a) Cyclic voltammetry using different windows (scan rate of 50 mV s^{-1}) (b) discharge curves at different rates and (c) capacity vs. cycle at different rates of a C/PB-AC device. (d) Photo of four C/PB-AC in series at (i) open and (ii) closed circuit to light a LED.

synthesized and processed as a self-standing thin film that can be easily deposited over any substrate, regardless of its material, shape and roughness (as observed in Fig. 4b and c).

In the current work, the focus was to explore the interfacial electron transfer process as means to produce a CNT/PB composite and further evaluate its performance as aqueous rechargeable potassium battery cathode, presenting a good capacity and rate handling even in non-optimised conditions. However, this synthetic method also allows exploration of different parameters, such as other conductive carbons assembled at the interface or post-process thermal treatments (as the material is binder-free) or device configurations using flexible and/or transparent substrates. In the C/PB-CA cell, there is a significant shift of the redox process of PB after several discharge cycles to $E_{1/2}$ ca. 0.70 V (Fig. 8a). However, in devices built with bare CNTs (CNT-CA) or AC (AC-AC), there are no significant changes in the voltammetric profiles before and after charge/discharge studies (after the stabilization of oxidation process of CNTs) that could explain such behaviour. These cells present a typical capacitor profile with triangle shaped curves (Fig. S8) with much lower capacities, confirming that the observed behaviour and capacities arise from PB in the composite. Due to the secondary process described previously, charging time during cycles is fairly high, giving low EC of 65%. Nevertheless, this effect is decreased and eliminated at higher discharge rates, as observed in Fig. 8c. The recovery at final cycles is about 84% of initial capacity, reaching 38 mAh g^{-1} at 0.25 A g^{-1}. This level of performance is comparable to some reported literature on PB-based electrodes in a full-cell setup, however this class of materials can reach impressive long-term stability with potassium [66], sodium [68] and ammonium [69] ions, amongst others [70]. Such stability is yet to be further optimised and tested with the material reported here. To demonstrate cell operation, four C/PB-AC devices connected in series and charged could light a white LED, as presented in Fig. 8d and the video in supplementary data.

Supplementary video related to this article can be found at https://doi.org/10.1016/j.electacta.2020.136243

4. Conclusions

From the presented data, the synthesis and application of CNT/PB obtained using a growth method at the L/L interface was demonstrated, and applied as the cathode of an aqueous rechargeable potassium battery. The characterization data confirm the preparation of a composite between CNTs and PB at the L/L interface, with the CNT scaffold acting as the nucleus for the deposition of the PB. The effect of DMFc on the synthesis of PB from acid decomposition of $[Fe(CN)_6]^{3-}$ was demonstrated for the first time, showing the viability of this process in the controlled chemical synthesis of PB and PB-based composites in a biphasic system. CNTs act as nucleation seeds as well as support for the formation of a self-assembled and continuous film at the L/L interface, indeed it is not possible to prepare a film in the absence of CNT. In addition, CNTs impart electronic conductivity to the composite, improving charge transport and charge injection into PB. The PB structure grows selectively over the CNT walls, maximizing the effect of CNTs and interaction between components, even without the addition of a binder material. Due to the redox properties of PB and conductivity of CNTs, the films could be applied as electrodes of aqueous batteries. The assembly of coin cell devices enabled evaluation of the performance in a full cell system, presenting significant capacities as aqueous potassium batteries. An AC anode was used without any optimization: this factor could further improve full cell performance. Furthermore, the preparation of the composites at the L/L interface allows them to be deposited over any desired substrate, for example the expansion of device design to transparent and flexible batteries is readily conceived.

Declaration of competing interest

The authors declare that they have no known competing financial interests or personal relationships that could have appeared to influence the work reported in this paper.

CRediT authorship contribution statement

Samantha Husmann: Data curation, Methodology, Formal analysis, Writing - original draft. **Aldo J.G. Zarbin:** Writing - original draft. **Robert A.W. Dryfe:** Writing - original draft.

Acknowledgements

We acknowledge the financial support from Brazilian and U.K research funding agencies CNPq, National Institute of Science and Technology of Carbon Nanomaterials (INCT-Nanocarbono) and EPSRC (grant references EP/R023034/1. EP/S019367/1, EP/P025021/1 and EP/N032888/1). This study was financed in part by the Coordenação de Aperfeiçoamento de Pessoal de Nível Superior – Brasil (CAPES) – Finance Code 001. S.H. thanks CAPES for the sandwich scholarship that enabled this collaboration.

Appendix A. Supplementary data

Supplementary data to this article can be found online at https://doi.org/10.1016/j.electacta.2020.136243.

References

[1] J. Liu, C. Xu, Z. Chen, S. Ni, Z.X. Shen, Progress in aqueous rechargeable batteries, Green Energy & Environment 3 (2018) 20–41.
[2] J.O.G. Posada, A.J. Rennie, S.P. Villar, V.L. Martins, J. Marinaccio, A. Barnes, C.F. Glover, D.A. Worsley, P.J. Hall, Aqueous batteries as grid scale energy storage solutions, Renew. Sustain. Energy Rev. 68 (2017) 1174–1182.
[3] N. Alias, A.A. Mohamad, Advances of aqueous rechargeable lithium-ion battery: a review, J. Power Sources 274 (2015) 237–251.
[4] H. Kim, J. Hong, K.-Y. Park, H. Kim, S.-W. Kim, K. Kang, Aqueous rechargeable Li and Na ion batteries, Chem. Rev. 114 (2014) 11788–11827.
[5] H. Kim, J. Hong, K.Y. Park, H. Kim, S.W. Kim, K. Kang, Aqueous rechargeable Li and Na ion batteries, Chem. Rev. 114 (2014) 11788–11827.
[6] B.J. Landi, M.J. Ganter, C.D. Cress, R.A. DiLeo, R.P. Raffaelle, Carbon nanotubes for lithium ion batteries, Energy Environ. Sci. 2 (2009) 638–654.
[7] K. Zaghib, J. Shim, A. Guerfi, P. Charest, K. Striebel, Effect of carbon source as additives in LiFePO4 as positive electrode for lithium-ion batteries, Electrochem. Solid State Lett. 8 (2005) A207–A210.
[8] H. Zheng, R. Yang, G. Liu, X. Song, V.S. Battaglia, Cooperation between active material, polymeric binder and conductive carbon additive in lithium ion battery cathode, J. Phys. Chem. C 116 (2012) 4875–4882.
[9] J. Qian, C. Wu, Y. Cao, Z. Ma, Y. Huang, X. Ai, H. Yang, Prussian blue cathode materials for sodium-ion batteries and other ion batteries, Adv. Energy Mater. 8 (17) (2018) 1702619.
[10] P. Nie, L. Shen, H. Luo, B. Ding, G. Xu, J. Wang, X. Zhang, Prussian blue analogues: a new class of anode materials for lithium ion batteries, J. Mater. Chem. 2 (2014) 5852–5857.
[11] Y. Xu, S. Zheng, H. Tang, X. Guo, H. Xue, H. Pang, Prussian blue and its derivatives as electrode materials for electrochemical energy storage, Energy Storage Materials 9 (2017) 11–30.
[12] B. Wang, Y. Han, X. Wang, N. Bahlawane, H. Pan, M. Yan, Y. Jiang, Prussian blue analogues for rechargeable batteries, iScience 3 (2018) 110–133.
[13] D.E. Stilwell, K.H. Park, M.H. Miles, Electrochemical studies of the factors influencing the cycle stability of Prussian Blue films, J. Appl. Electrochem. 22 (1992) 325–331.
[14] R. Garjonyte, A. Malinauskas, Operational stability of amperometric hydrogen peroxide sensors, based on ferrous and copper hexacyanoferrates, Sens. Actuators, B 56 (1999) 93–97.
[15] Z. Li, J. Chen, W. Li, K. Chen, L. Nie, S. Yao, Improved electrochemical properties of prussian blue by multi-walled carbon nanotubes, J. Electroanal. Chem. 603 (2007) 59–66.
[16] J. Li, J.D. Qiu, J.J. Xu, H.Y. Chen, X.H. Xia, The synergistic effect of prussian-blue-grafted carbon nanotube/poly(4-vinylpyridine) composites for amperometric sensing, Adv. Funct. Mater. 17 (2007) 1574–1580.
[17] J. Zhai, Y. Zhai, D. Wen, S. Dong, Prussian blue/multiwalled carbon nanotube

hybrids: synthesis, assembly and electrochemical behavior, Electroanalysis 21 (2009) 2207–2212.
[18] E. Nossol, A.B.S. Nossol, A.J.G. Zarbin, A.M. Bond, Carbon nanotube/Prussian blue nanocomposite film as a new electrode material for environmental treatment of water samples, RSC Adv. 3 (2013) 5393.
[19] M. Luo, Y. Dou, H. Kang, Y. Ma, X. Ding, B. Liang, B. Ma, L. Li, A novel interlocked Prussian blue/reduced graphene oxide nanocomposites as high-performance supercapacitor electrodes, J. Solid State Electrochem. 19 (2015) 1621–1631.
[20] S. Husmann, L.F. Lima, L.S. Roman, A.J.G. Zarbin, Photoanode for aqueous dye-sensitized solar cells based on a novel multicomponent thin film, ChemSusChem 11 (2018) 1238–1245.
[21] E. Nossol, A.J.G. Zarbin, Transparent films from carbon nanotubes/Prussian blue nanocomposites: preparation, characterization, and application as electrochemical sensors, J. Mater. Chem. 22 (2012) 1824–1833.
[22] Z. Chu, Y. Liu, W. Jin, Recent progress in Prussian blue films: methods used to control regular nanostructures for electrochemical biosensing applications, Biosens. Bioelectron. 96 (2017) 17–25.
[23] S. Husmann, A.J.G. Zarbin, Cation effect on the structure and properties of hexacyanometallates-based nanocomposites: improving cathode performance in aqueous metal-ions batteries, Electrochim. Acta 283 (2018) 1339–1350.
[24] S. Husmann, E.S. Orth, A.J.G. Zarbin, A multi-technique approach towards the mechanistic investigation of the electrodeposition of Prussian blue over carbon nanotubes film, Electrochim. Acta 312 (2019) 380–391.
[25] P.L. Domingo, B. García, J.M. Leal, Acid–base behaviour of the ferricyanide ion in perchloric acid media. Spectrophotometric and kinetic study, Can. J. Chem. 68 (1990) 228–235.
[26] R. Yang, Electrochemical deposition of prussian blue from a single ferricyanide solution, J. Electrochem. Soc. 145 (1998) 2231.
[27] D. Zhang, K. Wang, D. Sun, X. Xia, H. Chen, Potentiodynamic deposition of Prussian blue from a solution containing single component of ferricyanide and its mechanism investigation, J. Solid State Electrochem. 7 (2003) 561–566.
[28] S.S. Kumar, J. Joseph, K.L. Phani, Novel method for deposition of Gold–Prussian blue nanocomposite films induced by electrochemically formed gold nanoparticles: characterization and application to electrocatalysis, Chem. Mater. 19 (2007) 4722–4730.
[29] M.C. Schnitzler, M.M. Oliveira, D. Ugarte, A.J.G. Zarbin, One-step route to iron oxide-filled carbon nanotubes and bucky-onions based on the pyrolysis of organometallic precursors, Chem. Phys. Lett. 381 (2003) 541–548.
[30] R.V. Salvatierra, M.M. Oliveira, A.J.G. Zarbin, One-pot synthesis and processing of transparent, conducting, and freestanding carbon nanotubes/polyaniline composite films, Chem. Mater. 22 (2010) 5222–5234.
[31] D. Zhang, K. Wang, D. Sun, X. Xia, H.-Y. Chen, Ultrathin layers of densely packed Prussian blue nanoclusters prepared from a ferricyanide solution, Chem. Mater. 15 (2003) 4163–4165.
[32] Y.-L. Hu, J.-H. Yuan, W. Chen, K. Wang, X.-H. Xia, Photochemical synthesis of Prussian blue film from an acidic ferricyanide solution and application, Electrochem. Commun. 7 (2005) 1252–1256.
[33] F. Reymond, H.H. Girault, Electrochemistry at Liquid/Liquid Interfaces, Encyclopedia of Analytical Chemistry, Johcn Wiley & Sons, Ltd, 2006.
[34] R.A.W. Dryfe, Modifying the liquid/liquid interface: pores, particles and deposition, Phys. Chem. Chem. Phys. 8 (2006) 1869–1883.
[35] I. Noviandri, K.N. Brown, D.S. Fleming, P.T. Gulyas, P.A. Lay, A.F. Masters, L. Phillips, The decamethylferrocenium/decamethylferrocene redox couple: a superior redox standard to the ferrocenium/ferrocene redox couple for studying solvent effects on the thermodynamics of electron transfer, J. Phys. Chem. B 103 (1999) 6713–6722.
[36] M.B. Robin, The color and electronic configurations of prussian blue, Inorg. Chem. 1 (1962) 337–342.
[37] K. Itaya, I. Uchida, Nature of intervalence charge-transfer bands in Prussian blues, Inorg. Chem. 25 (1986) 389–392.
[38] B. Quinn, R. Lahtinen, L. Murtomäki, K. Kontturi, Electron transfer at micro liquid–liquid interfaces, Electrochim. Acta 44 (1998) 47–57.
[39] A. Uehara, S.-Y. Chang, S.G. Booth, S.L. Schroeder, J.F.W. Mosselmans, R.A. Dryfe, Redox and ligand exchange during the reaction of tetrachloroaurate with hexacyanoferrate (II) at a liquid-liquid interface: voltammetry and X-ray absorption fine-structure studies, Electrochim. Acta 190 (2016) 997–1006.
[40] S. Husmann, S.G. Booth, A.J.G. Zarbin, R.A.W. Dryfe, Electrodeposition of prussian blue/carbon nanotube composites at a liquid-liquid interface, J. Braz. Chem. Soc. 29 (2018) 1130–1139.
[41] P.S. Toth, A.K. Rabiu, R.A.W. Dryfe, Controlled preparation of carbon nanotube-conducting polymer composites at the polarisable organic/water interface, Electrochem. Commun. 60 (2015) 153–157.
[42] V.J. Cunnane, G. Geblewicz, D.J. Schiffrin, Electron and ion transfer potentials of ferrocene and derivatives at a liquid-liquid interface, Electrochim. Acta 40 (1995) 3005–3014.
[43] M.S. Dresselhaus, A. Jorio, R. Saito, Characterizing graphene, graphite, and carbon nanotubes by Raman spectroscopy, in: J.S. Langer (Ed.), Annual Review of Condensed Matter Physics vol. 1, Annual Reviews, Palo Alto, 2010, pp. 89–108.
[44] M.S. Dresselhaus, G. Dresselhaus, R. Saito, A. Jorio, Raman spectroscopy of carbon nanotubes, Phys. Rep. 409 (2005) 47–99.
[45] Y. Wang, D.C. Alsmeyer, R.L. McCreery, Raman spectroscopy of carbon materials: structural basis of observed spectra, Chem. Mater. 2 (1990) 557–563.
[46] X. Zhai, Z. Gao, Prussian blue electrodeposited on nano Ag-coated multiwalled carbon nanotubes composite for the determination of hydrogen peroxide, Anal. Sci. 26 (2010) 343–347.
[47] S.M. Golabi, F. Noor-Mohammadi, Electrocatalytic oxidation of hydrazine at cobalt hexacyanoferrate- modified glassy carbon, Pt and Au electrodes, J. Solid State Electrochem. 2 (1998) 30–37.
[48] F. Davodi, M. Tavakkoli, J. Lahtinen, T. Kallio, Straightforward synthesis of nitrogen-doped carbon nanotubes as highly active bifunctional electrocatalysts for full water splitting, J. Catal. 353 (2017) 19–27.
[49] P.S. Toth, A.N.J. Rodgers, A.K. Rabiu, D. Ibañez, J.X. Yang, A. Colina, R.A.W. Dryfe, Interfacial doping of carbon nanotubes at the polarisable organic/water interface: a liquid/liquid pseudo-capacitor, J. Mater. Chem. A 4 (2016) 7365–7371.
[50] C. Rao, R. Voggu, Charge-transfer with graphene and nanotubes, Mater. Today 13 (2010) 34–40.
[51] C. Lundgren, R.W. Murray, Observations on the composition of Prussian blue films and their electrochemistry, Inorg. Chem. 27 (1988) 933–939.
[52] F. Ricci, A. Amine, G. Palleschi, D. Moscone, Prussian Blue based screen printed biosensors with improved characteristics of long-term lifetime and pH stability, Biosens. Bioelectron. 18 (2003) 165–174.
[53] K. Itaya, I. Uchida, V.D. Neff, Electrochemistry of polynuclear transition metal cyanides: prussian blue and its analogues, Acc. Chem. Res. 19 (2002) 162–168.
[54] A. Dostal, B. Meyer, F. Scholz, U. Schroeder, A.M. Bond, F. Marken, S.J. Shaw, Electrochemical study of microcrystalline solid Prussian blue particles mechanically attached to graphite and gold electrodes: electrochemically induced lattice reconstruction, J. Phys. Chem. 99 (1995) 2096–2103.
[55] P. Kulesza, M. Malik, K. Miecznikowski, A. Wolkiewicz, S. Zamponi, M. Berrettoni, R. Marassi, Countercation-sensitive electrochromism of cobalt hexacyanoferrate films, J. Electrochem. Soc. 143 (1996) L10–L12.
[56] N.R. de Tacconi, K. Rajeshwar, R.O. Lezna, Metal hexacyanoferrates: electrosynthesis, in situ characterization, and applications, Chem. Mater. 15 (2003) 3046–3062.
[57] Q. Zhang, Z. Wang, S. Zhang, T. Zhou, J. Mao, Z. Guo, Cathode materials for potassium-ion batteries: current status and perspective, Electrochem. Energy Rev. 1 (2018) 625–658.
[58] J. Huang, Z. Guo, Y. Ma, D. Bin, Y. Wang, Y. Xia, Recent progress of rechargeable batteries using mild aqueous electrolytes, Small Methods 3 (2019) 1800272.
[59] H. Ao, Y. Zhao, J. Zhou, W. Cai, X. Zhang, Y. Zhu, Y. Qian, Rechargeable aqueous hybrid ion batteries: developments and prospects, J. Mater. Chem. A 7 (2019) 18708–18734.
[60] D. Su, A. McDonagh, S.Z. Qiao, G. Wang, High-capacity aqueous potassium-ion batteries for large-scale energy storage, Adv. Mater. 29 (2017) 1604007.
[61] C.D. Wessells, R.A. Huggins, Y. Cui, Copper hexacyanoferrate battery electrodes with long cycle life and high power, Nat. Commun. 2 (2011) 550.
[62] C.D. Wessells, S.V. Peddada, R.A. Huggins, Y. Cui, Nickel hexacyanoferrate nanoparticle electrodes for aqueous sodium and potassium ion batteries, Nano Lett. 11 (2011) 5421–5425.
[63] M. Pasta, C.D. Wessells, R.A. Huggins, Y. Cui, A high-rate and long cycle life aqueous electrolyte battery for grid-scale energy storage, Nat. Commun. 3 (2012) 1149.
[64] M. Jayalakshmi, F. Scholz, Performance characteristics of zinc hexacyanoferrate/Prussian blue and copper hexacyanoferrate/Prussian blue solid state secondary cells, J. Power Sources 91 (2000) 217–223.
[65] E. Ali, Potassium secondary cell based on Prussian blue cathode, J. Power Sources 126 (2004) 221–228.
[66] W. Ren, X. Chen, C. Zhao, Ultrafast aqueous potassium-ion batteries cathode for stable intermittent grid-scale energy storage, Adv. Energy Mater. 8 (2018) 1801413.
[67] D.S. Charles, M. Feygenson, K. Page, J. Neuefeind, W. Xu, X. Teng, Structural water engaged disordered vanadium oxide nanosheets for high capacity aqueous potassium-ion storage, Nat. Commun. 8 (2017) 15520.
[68] L. Zhou, Z. Yang, C. Li, B. Chen, Y. Wang, L. Fu, Y. Zhu, X. Liu, Y. Wu, Prussian blue as positive electrode material for aqueous sodium-ion capacitor with excellent performance, RSC Adv. 6 (2016) 109340–109345.
[69] C. Li, W. Yan, S. Liang, P. Wang, J. Wang, L. Fu, Y. Zhu, Y. Chen, Y. Wu, W. Huang, Achieving a high-performance Prussian blue analogue cathode with an ultra-stable redox reaction for ammonium ion storage, Nanoscale Horizons 4 (2019) 991–998.
[70] B. Wang, Y. Han, X. Wang, N. Bahlawane, H. Pan, M. Yan, Y. Jiang, Prussian blue analogs for rechargeable batteries, Iscience 3 (2018) 110–133.